AGU100 ADVANCING EARTH AND SPACE SCIENCE

Geophysical Research Letters

RESEARCH LETTER
10.1029/2018GL077551

Key Points:
- Three hundred-fold variations in the likelihood of induced seismicity can be estimated prior to injection
- Extensional and strike-slip settings, and especially transitional stress regimes, are the most susceptible
- Preinjection pore pressure is unimportant, so underpressured basins are not insulated from hazard

Correspondence to:
W. Levandowski,
bouldergeophysics@gmail.com

Citation:
Levandowski, W., Weingarten, M., & Walsh, R., III (2018). Geomechanical sensitivities of injection-induced earthquakes. *Geophysical Research Letters*, *45*, 8958–8965. https://doi.org/10.1029/2018GL077551

Received 14 FEB 2018
Accepted 29 JUN 2018
Accepted article online 5 JUL 2018
Published online 14 SEP 2018

Geomechanical Sensitivities of Injection-Induced Earthquakes

Will Levandowski[1], Matthew Weingarten[2,3], and Rall Walsh III[2,4]

[1]Department of Geology, Colorado College, Colorado Springs, CO, USA, [2]Department of Geophysics, Stanford University, Stanford, CA, USA, [3]Department of Geological Sciences, San Diego State University, San Diego, CA, USA, [4]Now at Decision Geomechanics, LLC, San Francisco, CA, USA

Abstract Wastewater reinjection increases pore fluid pressure and can make faults frictionally unstable, triggering earthquakes. Little is known, however, about how regional geomechanical properties influence the likelihood that disposal will induce seismicity. We investigate the impact of preinjection conditions on the proportion of possible fault orientations destabilized by a specified pore pressure increase. Stress state is the most important factor, with 7 times as many planes unstable in extension than contraction—indeed, normal or strike-slip faulting environments characterize most injection-induced seismicity—and additional fivefold increases in transitional stress states. Geomechanical susceptibility depends inversely on overburden density and depth, consistent with the shallow hypocenters of most induced events. The coefficient of friction and initial pore pressure have little impact: Faults initially below hydrostatic pressure can slip during gravity-fed injection. Combining these factors, site-specific geomechanical analyses could determine 300-fold variations in the likelihood of induced seismicity before disposal, offering a proactive way to manage hazard.

Plain Language Summary We investigate what factors influence the likelihood that industrial activities will trigger earthquakes. The initial pore-fluid pressure is unimportant, meaning that gravity-fed injection can readily cause seismicity. By contrast, readily known properties of the region (stress state, depth to bedrock faults, and density of the overlying sedimentary rock units) produce 300-fold variations in the likelihood of injection-induced earthquakes. Conducting simple analyses prior to injection could mitigate seismic hazard.

1. Introduction

Parts of the United States (Figure 1) have seen a dramatic increase in earthquake rates over the past decade because of industrial activities, especially disposal of wastewater from oil and gas operations into subsurface sedimentary rock (Ellsworth, 2013; Keranen et al., 2013; Rubinstein et al., 2014). Injected fluids can increase pore pressure on faults, leading to frictional instability and slip (Lee et al., 2016; National Research Council, 2013). Previous research has investigated the impact of well-operational parameters (e.g., Weingarten et al., 2015), meter-scale dynamics of induced moment release (e.g., Guglielmi et al., 2015), or the relative likelihood of slip on specific faults (Holland, 2013; Walsh III & Zoback, 2016), but less attention has been paid to what factors influence the susceptibility of a region as a whole to induced seismicity.

The mechanics of induced seismicity are well understood in the context of Mohr-Coulomb criteria. A given plane will become unstable when the pore pressure reaches a critical value such that the shear traction τ resolved on the plane overcomes frictional resistance (Hubbert & Rubey, 1959):

$$\tau = \mu\,(S_N - P_{crit}) + C \tag{1}$$

Frictional resistance is the product of the coefficient of friction μ and effective normal stress, which is the magnitude of the normal traction S_N minus the critical pore pressure P_{crit}. We will neglect cohesion at present because induced earthquakes generally reactivate existing faults (e.g., McNamara et al., 2015), which are thought to have little cohesive strength (e.g., Zoback, 2010). We will return to the possible effects of cohesion below.

For a fault in a region equilibrated to ambient preinjection pore pressure P_0, one can readily define the pressure perturbation required to make a given fault frictionally unstable:

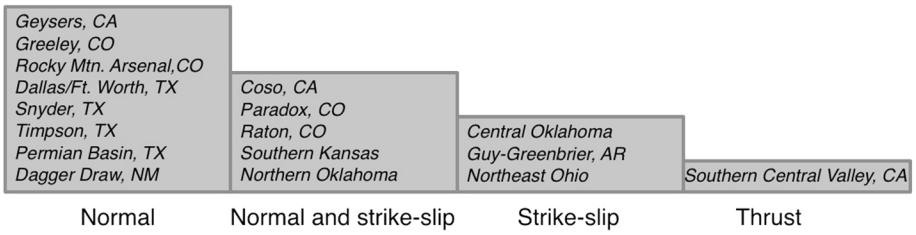

Figure 1. Areas of potentially induced earthquakes in the continental United States grouped by faulting style. Normal and strike-slip faulting appear more common than induced thrust faulting.

$$\Delta P \equiv P_{crit} - P_0 = S_N - \tau/\mu - P_0 \tag{2}$$

On a Mohr diagram, ΔP is the horizontal distance from the failure envelope (e.g., Figure 2).

Recently, Walsh III and Zoback (2016) investigated the risk of triggered slip (i.e., reaching frictional instability) on mapped faults in northern and central Oklahoma. As with Holland (2013), primary attention was paid to the influence of fault orientation relative to local stress directions, but conditional probabilities were also quantified by considering uncertainty in stress directions and stress ratio (based on inversions of focal mechanisms), friction, P_0, and overburden density. In a Monte Carlo fashion, values from posterior or assumed distributions of each parameter were combined to derive the full stress tensor, the normal and shear tractions resolved onto mapped fault planes, and the values of ΔP calculated. Hypocentral depths were set to 5 km, fault dips were assumed to be near vertical, and—because Walsh III and Zoback's (2016) objective was specific to northern and central Oklahoma—only mapped faults were considered.

Aside from fault orientation relative to the local stress field, however, the impacts of the other parameters have not been determined. Moreover, detailed fault maps are not available in all areas: Even in Oklahoma, both the M5.1 Fairview and M5.8 Pawnee earthquakes occurred on unmapped fault segments (Yeck et al., 2016, 2017). Because any given region is likely to have inherited faults of many orientations, our analysis assumes no knowledge of fault orientations relative to principal stress directions and instead investigates the extent to which it is possible to determine regional susceptibility to injection-induced earthquakes as a function of geomechanical parameters at the hypocenter. Specifically, the proportion of all possible fault orientations that would be frictionally unstable after a specified pore pressure increase is quantified as functions of faulting environment, stress ratio, hypocentral depth, overburden density, friction, and ambient (long-term, preinjection) pore pressure.

2. Deriving the Full Stress Tensor

In order to calculate shear and normal tractions (and hence ΔP), the magnitudes of the three principal stresses must be known. These magnitudes can be computed from P_0, μ, hypocentral depth, overburden density, faulting environment, and stress ratio as follows.

If frictional failure equilibrium holds, then an optimally oriented fault is critically stressed at ambient pore pressure:

$$\tau_{\mathrm{opt}} = \mu \left(S_{Nopt} - P_0 \right) \tag{3}$$

For this optimal fault, ΔP is 0; this plane plots where the failure envelope is tangential to the Mohr circle. (In the present context, P_0 refers to the pore pressure to which faults have equilibrated; the discussion below is applicable to naturally underpressured regions, not to pressure-depleted reservoirs in which anthropogenic removal of fluids has decreased pore pressure.) Following Zoback (2010), equation (3) implies the relationship between the magnitudes of the maximally compressive stress S_1 and minimally compressive stress S_3:

$$(S_1 - P_0)/(S_3 - P_0) = \left[\sqrt{\left(\mu^2 + 1\right)} + \mu\right]^2 \equiv \Upsilon \tag{4}$$

Vertical normal stress at depth z depends on the average density of overburden ρ:

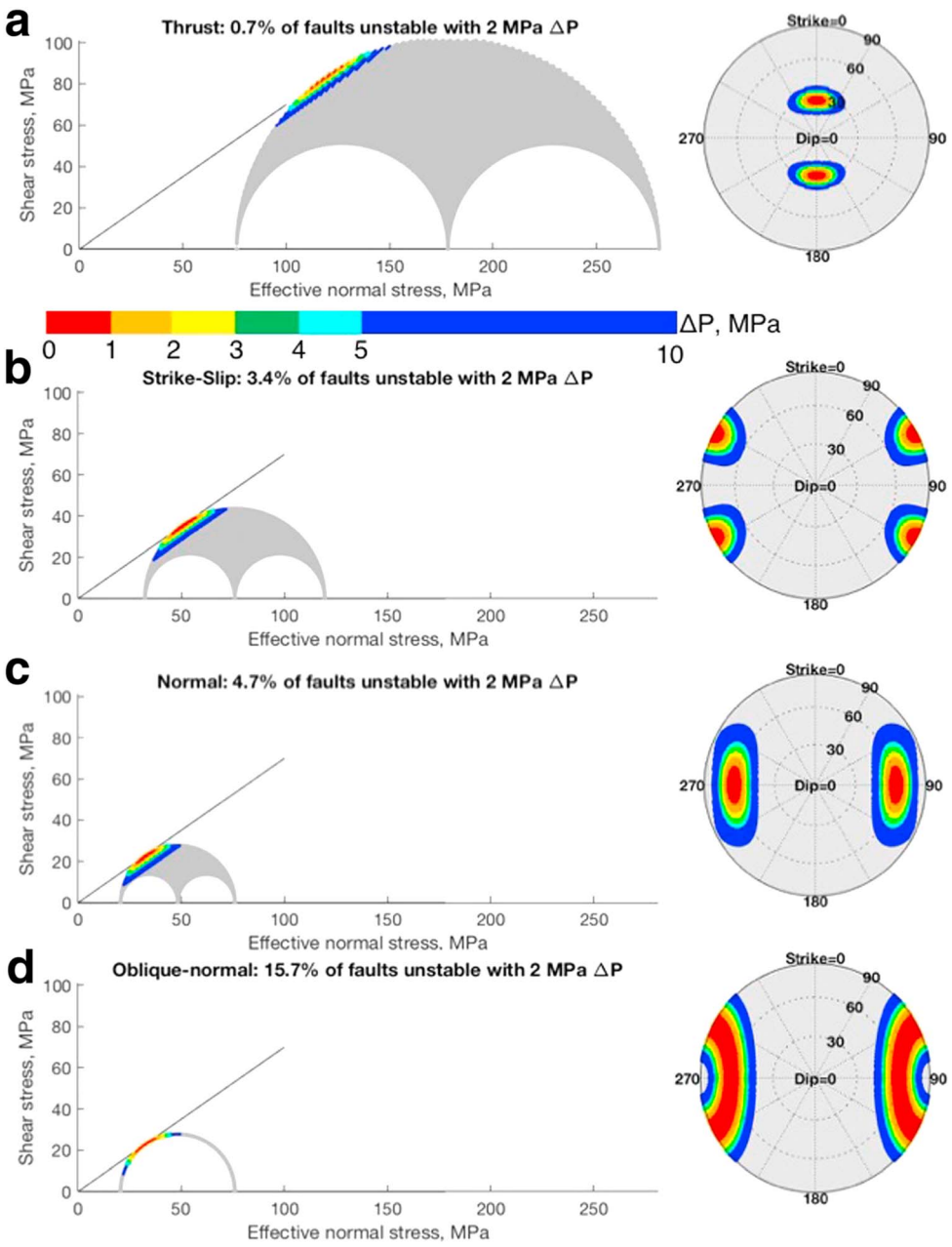

Figure 2. Mohr circles and stereonets of different faulting regimes. (a) Thrust faulting environment with Φ = 0.5, depth = 5 km, overburden density of 2,500 kg/m^3, μ = 0.7, and hydrostatic P_0. Of all possible fault orientations, 0.7% would be frictionally stable with a 2-MPa pressure increase. These are ~30°-dipping, ~N-S-striking planes (see right panel). Color bar depicts ΔP and is the same in all panels. Axes are the same in all panels. (b) Strike-slip environment with the same properties: 3.4% of planes would be unstable with a 2-MPa pressure increase. (c) Normal faulting: 4.7% of planes would be unstable. (d) Oblique-normal faulting environment: Φ = 1. Rather than intermediate between strike slip and normal susceptibility, the proportion of unstable planes jumps to 15.7%. This spike occurs because pure dip-slip, pure strike-slip, and oblique-slip faults are all nearly optimally oriented.

$$S_V = \rho g z \tag{5}$$

In normal, strike-slip, and thrust faulting environments, S_V can be substituted for S_1, S_2, and S_3, respectively. Combining equations (4) and (5) with the stress ratio Φ (following Angelier, 1990) provides three equations that can be solved simultaneously for the magnitudes of the three principal stresses:

$$\phi = (S_2 - S_3)/(S_1 - S_3) \quad (6)$$

For practical applications, one could use focal mechanism stress inversions to solve for Φ and the faulting environment, as well as to determine horizontal principal stress directions (which in the present analysis are arbitrary).

Perhaps the simplest illustration of the derivation of the full stress tensor is for a state of stress that is transitional between normal and strike-slip faulting ($S_V = S_1 = S_2$). This transitional style of faulting is similar to that observed in southern Kansas and northern Oklahoma (Levandowski et al., 2018; Walsh III & Zoback, 2016; Figure 1). Equation (4) gives the final principal stress magnitude:

$$S_3 = P_0 + (S_V - P_0)/\gamma \quad (7)$$

Similarly, in different faulting environments the value of S_V takes the place of one of the principal stresses, and equations (4)–(6) are combined. For example, in a normal faulting regime, $S_V = S_1$ as above and S_3 is given by equation (7). Substituting into equation (6):

$$S_2 = (1 - \phi)S_3 + \phi S_1 \rightarrow S_2 = (1 - \phi)\,(P_0 + (S_V - P_0)/\gamma) + \phi S_V \quad (8)$$

Multiplying the unit vectors of the three principal stresses by their respective magnitudes gives the full stress tensor **σ**. For a fault of interest with a normal vector ***n***, the traction vector ***t*** produced by **σ** is ***σn***. The magnitude of the normal component gives S_N:

$$S_N = \boldsymbol{tn} \quad (9)$$

The shear traction vector ***τ*** is given as the cross product of ***n*** with the normal vector to the plane that contains ***t*** and ***n***.

$$\boldsymbol{\tau} = n \times (\boldsymbol{t} \times \boldsymbol{n}) \quad (10)$$

The shear traction magnitude τ is simply the magnitude of ***τ***. Finally, combining equations (2), (9), and (10) solves for ΔP for the fault in question.

To determine regional susceptibility to induced seismicity, and presuming no exhaustive knowledge of the orientations of existing fault planes, the following discussion repeats this process for a set of 20,000 planes that sample the focal sphere evenly. Then, the six geomechanical parameters are systematically varied to quantify their influences.

3. Influences of Geomechanical Factors

3.1. Stress Regime

The first set of solutions is derived for hydrostatic P_0, z = 5 km, μ = 0.7, ρ = 2,500 kg/m^3, and Φ = 0.5, but faulting environment varies from normal to strike slip to reverse. Stress directions are arbitrary, and results are illustrated with maximal horizontal compression-oriented E-W. Because the magnitude of S_V is held constant, the diameter of the Mohr circle depends on whether S_V represents the maximal, intermediate, or minimal stress, and increases from normal to strike slip to reverse (Figure 2). Consequently, the proportion of fault orientations within some value of ΔP of failure decreases: 4.7% of faults in an extensional environment would be frictionally unstable after a 2-MPa pressure increase (in this case, ~60°-dipping, E-W-striking planes; Figure 2a), compared with 3.4% under strike slip and 0.7% in a thrust setting (Figure 1c). Therefore, faulting environment accounts for approximately sevenfold variation in susceptibility to induced seismicity.

These results are thought provoking in light of the fact that nearly all concentrations of induced seismicity in the United States (Figure 1) occur in normal or strike-slip environments (unless otherwise noted, the following are shown by Herrmann, 2017; Levandowski et al., 2018). Normal faulting dominates the Geysers and Coso fields in California; Paradox Valley, the Raton Basin, Greeley, and Rocky Mountain

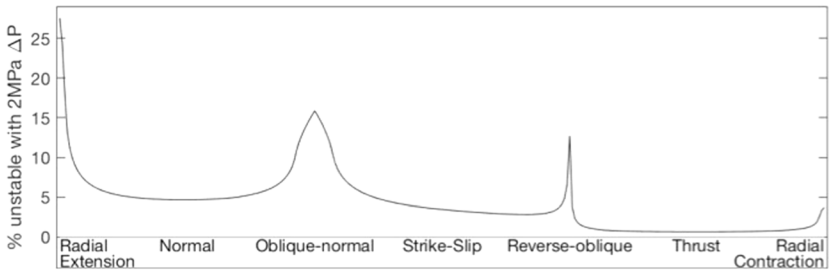

Figure 3. Proportions of faults destabilized by a 2-MPa pore pressure increase. There is a general decrease from extension to contraction, with superimposed jumps in transitional stress states.

Arsenal in Colorado; Dallas/Fort Worth (Hornbach et al., 2015), Snyder, Timpson (Fan et al., 2016), and the Permian Basin (Doser et al., 1991) in Texas; Dagger Draw in New Mexico; and southern Kansas. Oblique-normal faulting in northern Oklahoma grades toward strike slip, but ϕ remains greater than 0.5 (i.e., S_V is closer to S_1 than S_3; Levandowski et al., 2018; Walsh III & Zoback, 2016). Guy-Greenbrier, Arkansas, and eastern Ohio host pure strike-slip faulting, but no major examples of dominantly reverse motion induced by wastewater injection are documented in the United States, though one sequence of thrust earthquakes in the southern Central Valley, CA, appears to be related to wastewater injection (Goebel et al., 2016). Stress regime may be observationally biased if oil and gas development, and therefore wastewater reinjection sites, are more prevalent in extensional settings. Nevertheless, geomechanical susceptibility is higher in normal than strike-slip than thrust environments, providing a simple explanation for the predominance of induced normal faulting.

The second component of the stress regime is the stress ratio Φ. In fact, Simpson (1997) established a single quantitative parameter $A\Phi$ to describe the full stress regime:

$$A\phi = (n + 0.5) + (-1)^n(\phi - 0.5) \tag{11}$$

In equation (11), n is 0 for normal faulting, 1 for strike slip, and 2 for thrust (Zoback, 1992). Consequently, $A\Phi$ represents the continuum from radial extension ($A\Phi = 0$) to radial contraction ($A\Phi = 3$). Integer values of $A\Phi$ imply that two of the principal stresses are equal in magnitude. In such a situation, all faults plot along the outer edge of the Mohr circle (Figure 2d), and susceptibility to induced seismicity increases several times. For example, in an oblique-normal faulting environment ($S_1 = S_2 = S_V$, $A\Phi = 1$), 15.7% of faults are frictionally unstable after a 2-MPa pressure perturbation (Figure 2a), compared with 4.7% and 3.4% in normal and strike slip, respectively. Thus, there are additional approximately fivefold peaks in transitional stress states—most pronounced when $\Phi < 0.1$ or $\Phi > 0.9$—superimposed on the sevenfold decrease in susceptibility from extension to contraction. All told, there is nearly 40-fold variation in susceptibility (radial extension compared versus pure thrust faulting) that arises due to stress regime alone (Figure 3).

3.2. Depth and Overburden Density

As discussed above, the magnitude of vertical stress controls the magnitudes of principal stress and, as a result, the overall differential stress (represented by the diameter of the Mohr circle) and susceptibility to injection-induced earthquakes. Performing the same analyses as displayed in Figure 2 for different hypocentral depths (red lines in Figure 4a) reveals that halving depth (from 5 to 2.5 km) doubles the proportion of unstable faults in most stress regimes; doubling depth (to 10 km) halves susceptibility (Figure 4b). As such, susceptibility to slip is roughly a function of (hypocentral depth)$^{-1}$. Induced earthquakes typically occur on faults in the crystalline basement (e.g., McNamara et al., 2015), so this depth would correspond to depth to faulted bedrock. Thus, in addition to being closer to wellheads, shallow faults are geomechanically more prone to slip when subjected to a given pore pressure increase. Similarly, lower density overburden increases susceptibility: Faults beneath 2,000-kg/m^3 sediments (blue line in Figure 4a) are ~50% more susceptible than faults beneath 2,500-kg/m^3 sedimentary rock.

We caution that the inverse dependence of susceptibility on depth does not imply immunity to hazard from deeper faults. In fact, most moderate magnitude-induced seismicity occurs on faults several kilometers into

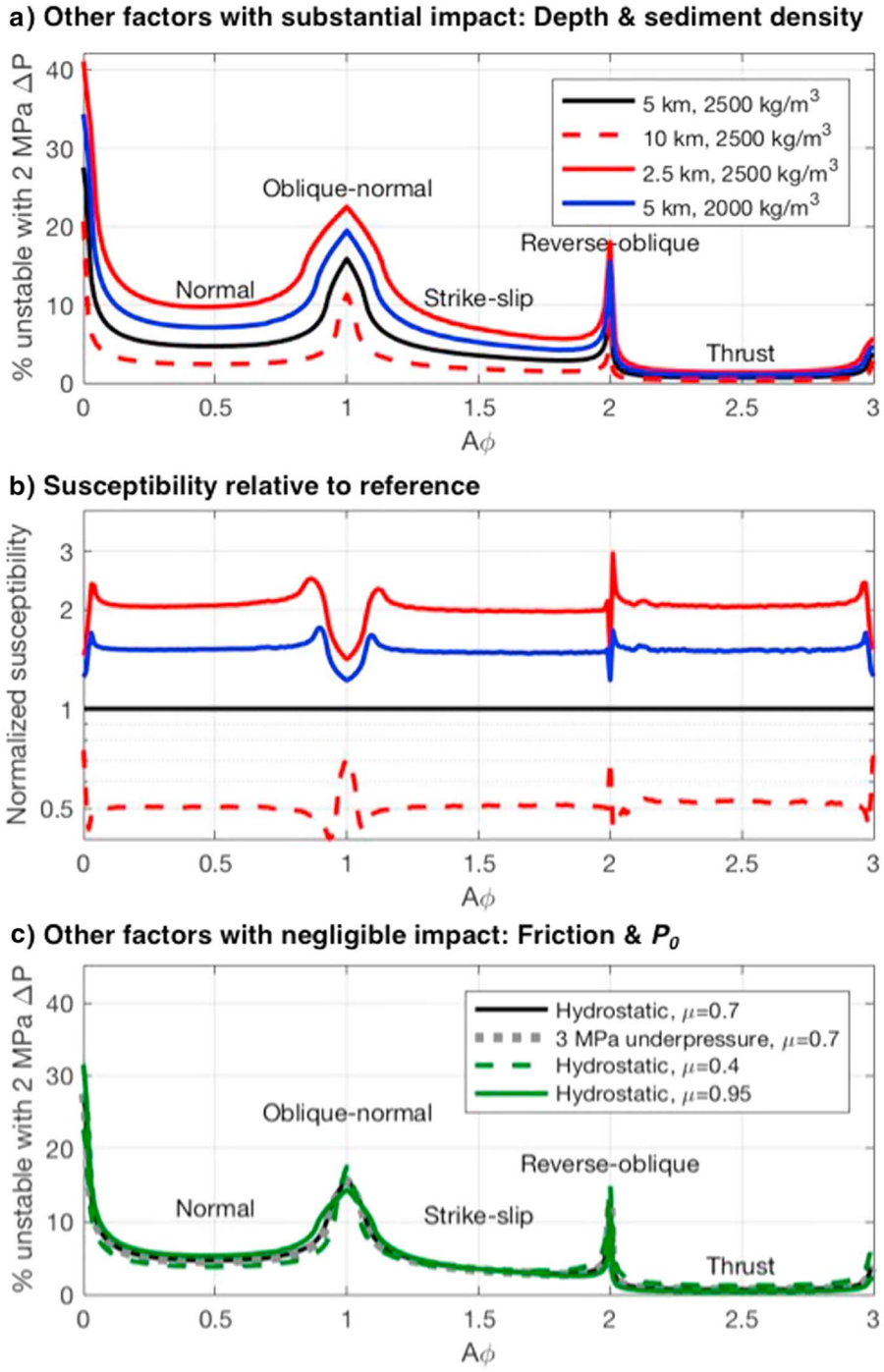

Figure 4. Sensitivities to other factors. (a) Susceptibility versus $A\Phi$, including variations in depth and overburden density. Black line depicts the same set of parameters as Figure 2b. Shallower faults (solid red line) are more susceptible, deeper faults (dashed red line) less. Lower-density overburden (blue line) also raises susceptibility. (b) Curves from (a) normalized by the black curve to emphasize relative susceptibility. For example, halving depth from 5 to 2.5 km generally doubles susceptibility. (c) Same as (a) but varying friction and initial pore pressure. Higher/lower friction (dashed/solid green lines) and underpressured formations (gray line) do not substantially affect susceptibility.

the crystalline basement (e.g., McNamara et al., 2015), where ambient differential stress is sufficiently high to cause potentially damaging shaking. Therefore, the probability of triggered slip decreases with fault depth, but the seismic hazard posed by induced seismicity may not.

3.3. Cohesion

Thus far, we have ignored the effect of cohesion, but the effects of weight per area of overburden serve as a template for understanding its impact. Increasing overburden increases normal stress on all faults, therefore increasing the overall differential stress (i.e., the radius of the Mohr circle) and decreasing the proportion of planes within some distance of the failure envelope. The impact of cohesion is the same: It allows for higher differential stress. We have conducted analyses including cohesion, and just as with depth and density, the impact across faulting regimes is consistent. Adding cohesion of 50 MPa with hydrostatic P_0, z = 5 km, μ = 0.7, and ρ = 2,500 kg/m^3 approximately halves the proportions of faults within 2 MPa of failure in all stress regimes.

3.4. Friction

The coefficient of friction controls optimal fault orientations in a given stress field, but performing identical analyses for reasonable ranges of static friction demonstrates that it does not substantially affect the proportion of faults that become unstable after some pore pressure increase (Figure 4c). Across all stress regimes, susceptibility is roughly the same for low μ (0.4, dashed green line), intermediate μ (0.7, solid black line), and high μ (0.9, solid green line). Thus, the impact of friction is to alter which fault planes are closest to failure, but we find that the coefficient of friction does not substantially alter how many possible planes are within a few megapascals of failure.

3.5. Initial Pore Pressure

The final parameter to investigate is P_0, which is of particular interest because reservoirs with subhydrostatic pore fluid pressures provide efficient disposal targets. Two of the most prominent examples of induced seismicity, however—central/northern Oklahoma to southern Kansas (Keranen et al., 2013) and the Raton Basin, Colorado (Rubinstein et al., 2014)—occur on basement faults beneath naturally underpressured basins (Nelson et al., 2015). Thus, understanding the extent to which underpressure does or does not decrease hazard of injection-induced instability is key to optimizing disposal while managing risk.

We specifically investigate the effect of hypocentral pore fluid pressure and implicitly assume pressure equilibrium between basement faults and overlying basins. If such a connection does not exist, it is the pressure in the seismogenic basement that is of importance in the equations above.

At a depth of 5 km, μ = 0.7, and overburden density of 2,500 kg/m^3, equations (4)–(6) are solved for an initial underpressure of 3 MPa (i.e., a pressure gradient that is 0.6 MPa/km below hydrostatic), approximately what is documented in the Arbuckle group of central/northern Oklahoma (Nelson et al., 2015) and—by assumption—underlying basement. Essentially the same proportion of faults are frictionally unstable after a certain pressure increase (gray line in Figure 4c) as in an initially hydrostatic basin. In an oblique-normal environment similar to that documented in northern Oklahoma, up to 15.7% of all possible fault orientations would be unstable following a 2-MPa pressure increase (i.e., while pore pressure remains 1 MPa below hydrostatic). Initially underpressured basins confer no protection from the hazard of injection-induced seismicity, and slip can be induced even during gravity-driven injection.

4. Discussion/Conclusion

The analyses performed above are simple and intentionally reductionist; more detailed models that include effects such as poroelasticity, fluid diffusion and flow, and water-rock interactions are needed in order to manage injection at specific sites. What the results here demonstrate, however, is that in critically stressed crust, site-specific geomechanical parameters create a 300-fold variation in susceptibility to induced seismicity simply from the combined impacts of stress regime, depth to basement faults, and density of sedimentary units. The implication of this finding is that, even without undertaking complex hydrogeologic modeling, one can estimate the relative susceptibility of a region to induced seismicity prior to injection, whether after injection is started, during the permitting process, or in the planning phase of reservoir development. Such estimation offers an easy and proactive way to appraise and manage hazard.

Our findings retrospectively explain several patterns of induced seismicity in the United States. (1) It is not coincidental that nearly all injection-induced seismicity has occurred in normal to strike-slip settings: Such areas are several times more likely to host a fault oriented such that instability will occur after a small pore

pressure increase. (2) It is not surprising that injection-induced earthquakes tend to be shallower than natural events (Boyd et al., 2017): In addition to being closer to the pressurized wells, shallower faults are geomechanically more susceptible to slip than relatively deeper faults. (3) It is not puzzling that much induced seismicity has occurred in underpressured basins: Underpressure basins does not insulate from injection-induced hazard because faults equilibrated to criticality under the preexisting underpressure are readily available to slip. The analyses presented here provide a framework for considering regional-scale susceptibility to induced earthquakes to aid designing disposal wells to minimize hazard.

Acknowledgments
Andrew Barbour provided comments on this manuscript prior to submission. The authors thank Cliff Frohlich, an anonymous reviewer, and Associate Editor Gavin Hayes. M. W. was supported by the Stanford Center for Induced and Triggered Seismicity. The analytical codes (in MATLAB) are available from W. L. All data used in this paper came from published sources listed in the references.

References

Angelier, J. (1990). Inversion of field data in fault tectonics to obtain the regional stress—III. A new rapid direct inversion method by analytical means. *Geophysical Journal International*, *103*, 363–376. https://doi.org/10.1111/j.1365-246X.1990.tb01777

Boyd, O. S., McNamara, D. E., Hartzell, S., & Choy, G. (2017). Influence of lithostatic stress on earthquake stress drops in North America. *Bulletin of the Seismological Society of America*, *107*(2), 856–868. https://doi.org/10.1785/0120160219

Doser, D. I., Baker, M. R., & Mason, D. B. (1991). Seismicity in the War-Wink gas field, Delaware Basin, west Texas, and its relationship to petroleum production. *Bulletin of the Seismological Society of America*, *81*(3), 971–986. https://doi.org/10.1016/0148-9062(92)93679-E

Ellsworth, W. L. (2013). Injection-induced earthquakes. *Science*, *341*(6142), 1225942. https://doi.org/10.1126/science.1225942

Fan, Z., Eichhubl, P., & Gale, J. F. W. (2016). Geomechanical analysis of fluid injection and seismic fault slip for the M_w4.8 Timpson, Texas, earthquake sequence. *Journal of Geophysical Research: Solid Earth*, *121*, 2798–2812. https://doi.org/10.1002/2016JB012821

Goebel, T. H. W., Hosseini, S. M., Cappa, F., Hauksson, E., Ampuero, J. P., Aminzadeh, F., & Saleeby, J. B. (2016). Wastewater disposal and earthquake swarm activity at the southern end of the Central Valley, California. *Geophysical Research Letters*, *43*, 1092–1099. https://doi.org/10.1002/2015GL066948

Guglielmi, Y., Cappa, F., Avouac, J.-P., Henry, P., & Elsworth, D. (2015). Seismicity triggered by fluid injection–induced aseismic slip. *Science*, *348*, 1224–1226.

Herrmann, R. (2017). SLU North America moment tensor catalog in CSV format with TABS separating columns. Retrieved from http://www.eas.slu.edu/eqc/eqc_mt/MECH.NA/MECHFIG/mech.html. (August 2017).

Holland, A. A. (2013). Optimal fault orientations within Oklahoma. *Seismological Research Letters*, *84*, 876–890.

Hornbach, M. J., DeShon, H. R., Ellsworth, W. L., Stump, B. W., Hayward, C., Frohlich, C., et al. (2015). Causal factors for seismicity near Azle, Texas. *Nature Communications*, *6*(1), 6728. https://doi.org/10.1038/ncomms7728

Hubbert, M. K., & Rubey, W. W. (1959). Role of fluid pressure in mechanics of overthrust faulting. *Geological Society of America Bulletin*, *70*(2), 115–166. https://doi.org/10.1130/0016-7606(1959)70[115:ROFPIM]2.0.CO;2

Keranen, K. M., Savage, H. M., Abers, G. A., & Cochran, E. S. (2013). Potentially induced earthquakes in Oklahoma, USA: Links between wastewater injection and the 2011 Mw 5.7 earthquake sequence. *Geology*, *41*(6), 699–702. https://doi.org/10.1130/G34045.1

Lee, J. Y., Weingarten, M., & Ge, S. (2016). Induced seismicity: The potential hazard from shale gas development and CO2 geologic storage. *Geosciences Journal*, *20*(1), 137–148. https://doi.org/10.1007/s12303-015-0030-5

Levandowski, W., Herrmann, R. B., Boyd, O. S., Briggs, R., & Gold, R. (2018). A revised stress map of the continental United States reveals heterogeneous intraplate stress. *Nature Geoscience*, *11*(6), 433–437. https://doi.org/10.1038/s41561-018-0120-x

McNamara, D. E., Benz, H. M., Herrmann, R. B., Bergman, E. A., Earle, P., Holland, A., et al. (2015). Earthquake hypocenters and focal mechanisms in central Oklahoma reveal a complex system of reactivated subsurface strike-slip faulting. *Geophysical Research Letters*, *42*, 2742–2749. https://doi.org/10.1002/2014GL062730

National Research Council (2013). *Induced seismicity potential in energy technologies* (p. 262). Washington, DC: The National Academies Press. https://doi.org/10.17226/13355

Nelson, P. H., Gianoutsos, N. J., & Drake, R. M. II (2015). Underpressure in Mesozoic and Paleozoic rock units in the Midcontinent of the United States. *AAPG Bulletin*, *99*(10), 1861–1892. https://doi.org/10.1306/04171514169

Rubinstein, J. L., Ellsworth, W. L., McGarr, A., & Benz, H. M. (2014). The 2001–present induced earthquake sequence in the Raton Basin of northern New Mexico and southern Colorado. *Bulletin of the Seismological Society of America*, *104*(5), 2162–2181.

Simpson, R. W. (1997). Quantifying Anderson's fault types. *Journal of Geophysical Research*, *102*(B8), 17,909–17,919. https://doi.org/10.1029/97JB01274

Walsh, F. R. III, & Zoback, M. D. (2016). Probabilistic assessment of potential fault slip related to injection-induced earthquakes: Application to north-central Oklahoma, USA. *Geology*, *44*(12), 991–994. https://doi.org/10.1130/G38275.1

Weingarten, M., Ge, S., Godt, J. W., Bekins, B. A., & Rubinstein, J. L. (2015). High-rate injection is associated with the increase in U.S. mid-continent seismicity. *Science*, *348*.

Yeck, W. L., Hayes, G. P., McNamara, D. E., Rubinstein, J. L., Barnhart, W. D., Earle, P. S., & Benz, H. M. (2017). Oklahoma experiences largest earthquake during ongoing regional wastewater injection hazard mitigation efforts. *Geophysical Research Letters*, *44*, 711–717. https://doi.org/10.1002/2016GL071685

Yeck, W. L., Weingarten, M., Benz, H. M., McNamara, D. E., Bergman, E. A., Herrmann, R. B., et al. (2016). Far-field pressurization likely cause one of the largest injection induced earthquakes by reactivating a large preexisting basement fault structure. *Geophysical Research Letters*, *43*(19), 10,198–10,207. https://doi.org/10.1002/2016GL070861

Zoback, M. D. (2010). *Reservoir geomechanics*. New York: Cambridge University Press.

Zoback, M. L. (1992). Stress field constraints on intraplate seismicity in eastern North America. *Journal of Geophysical Research*, *97*(B8), 11,761–11,782. https://doi.org/10.1029/92JB00221